

# On the comparison of strain measurements from fibre optics with dense seismometer array at Etna volcano (Italy)

Gilda Currenti<sup>1</sup>, Philippe Jousset<sup>2</sup>, Rosalba Napoli<sup>1</sup>, Charlotte Krawczyk<sup>2,3</sup>, Michael Weber<sup>2,4</sup>

5 <sup>1</sup>Istituto Nazionale di Geofisica e Vulcanologia-Osservatorio Etneo, Piazza Roma 2, Catania, Italy

<sup>2</sup>GFZ German Research Centre for Geosciences, Telegrafenberg, Potsdam 14473, Germany

<sup>3</sup>Technical University Berlin, Ernst-Reuter-Platz 1, Berlin10587, Germany

<sup>4</sup>University Potsdam, Karl-Liebknecht-Str. 24-25, Potsdam 14476, Germany

10 *Correspondence to:* Gilda Currenti (gilda.currenti@ingv.it)

**Abstract.** We demonstrate the capability of Distributed Acoustic Sensing (DAS) in recording volcano related dynamic strain at Etna (Italy). In summer 2019, we gathered DAS measurements from a 1.5 km long fibre in a shallow trench and seismic records from a conventional dense array comprising 26 broadband sensors, deployed in Piano delle Concazze close to the summit area. Etna activity during the acquisition period gives the extraordinary opportunity to record dynamic strain changes (few  $10^{-8}$  strain) in correspondence with volcanic events. To validate the DAS strain measurements, we explore array-derived methods to estimate strain changes from the seismic signals and to compare with strain DAS signals. A general good agreement is found between array-derived strain and DAS measurements along the fibre optic cable. Short wavelength discrepancies correspond with fault zones, showing the potential of DAS in mapping local perturbations of the strain field, and thus site effect, due to small-scale heterogeneities in volcanic settings.

## 20 1 Introduction

In the recent past, direct measures of the strain field have been hampered by the complex installation and high maintenance cost of conventional strainmeters. In the best case, few instruments are deployed in borehole, thus sensing the strain in only few points (Currenti and Bonaccorso, 2019). Numerical investigations have clearly shown that seismic velocities, gradient displacements and strain dramatically changes at sharp boundaries and in presence of steep topography (Kumagai et al., 2011; 25 Jousset et al., 2004; Cao and Mavroeidis, 2019). This poses challenges in interpreting accurately strain observations relying on only few measurements points.

Nowadays, advances in the direct measurement of strain at an unprecedented high spatial and temporal sampling over a broad frequency range have become possible due to the growing use of Distributed Acoustic Sensing (DAS) technology. Since the application of DAS in geoscience is an emerging field, many open questions still exist on the DAS device response and the 30 coupling effect between the fibre and the ground, that strongly depends on conditions of fibre installation (Ajo-Franklin et al.,

2019; Reinsch et al., 2017). A few field experiments in various environments have been designed to compare DAS strain measures and indirect strain estimates from collocated or nearby traditional sensors, such as geophones and broadband seismometers (Jousset et al., 2018; Wang et al., 2018; Yu et al., 2019; Lindsey et al., 2020).

In this paper we compare array-derived strain with direct strain DAS data, acquired at Etna volcano (Italy). As test site we selected Etna for its various and frequent activity. Lava flows, explosive eruptions with ash plumes, and strombolian lava fountains commonly occur from Etna summit craters and these multiple episodes of different style results in a wide variety of signals (Bonaccorso et al., 2004). A dense seismic array and a 1.5 km long fibre optic cable connected to a DAS interrogator were jointly installed few kilometers away from the summit craters to assess the reliability of DAS in recordings volcano related strain changes. To validate the DAS measurements, we explore several methods for the indirect estimates of strain field from dense seismic array data.

40 Several methods exist in literature for estimating strain from high to quasi-static frequencies relevant for seismologic and geodetic investigations. Those include the evaluation of seismic rotational components (Basu et al., 2013), the analysis of the performance of rotational seismometers (Suryanto et al., 2006), the estimation of strain-meter response and calibration (Donner et al., 2017; Currenti et al., 2017), the computation of strain rate maps (Teza et al., 2004; Shen et al., 2015), the estimation of 45 the stress field induced by the passage of seismic waves (Spudich et al., 1995), the determination of seismic phase velocity (Gomberg and Agnew, 1996; Spudich and Fletcher, 2008) and the estimates of wave attributes (Langston and Liang, 2008).

45 In general, those methods can be grouped in two main families relying on single or multiple station methods. On one hand, the single station method, pertinent only to seismology, has been widely used to estimate dynamic gradient displacements and strain tensor from the translational components of a 3C seismometer (Gomberg and Agnew, 1996). It assumes that seismic energy is carried by plane waves with known horizontal velocity in a laterally homogeneous medium. On the other hand, 50 multiple station procedures involve the use of displacements or velocity recordings from a number of close sensors (at least three; Basu et al., 2013; Currenti et al., 2017) or dense arrays (from tens to thousands sensors with short spacing going from tens to hundreds meters). The density and number of stations depends on the objectives of the array (Basu et al., 2017). In such a case, the measurements are processed using spatial interpolation approaches (Sandwell, 1987; Paolucci and Smerzini, 2008; 55 Sandwell and Wessel, 2016) or the well-known seismo-geodetic method (Spudich et al., 1995; Shen et al., 2015; Teza et al. 2004; Basu et al., 2013). Beside the use of geostatistical approaches, generally applied for optimal interpolation of a discrete scalar field, several interpolation schemes have been formulated using the solutions of suitable elasticity problems (Sandwell, 1987; Wessel and Bercovici, 1998; Paolucci and Smerzini, 2008). A complete review of these latter methods can be found in Sandwell and Wessel (2016). In the same paper the Authors, following the biharmonic spline method (Sandwell, 1987), 60 proposed a new solution, in which the interpolation functions originate from the computations of the analytic Green's solutions of an elastic body subjected to in-plane forces. Finally, the seismo-geodetic method is based on the Taylor expansions of the displacements field of first (Spudich et al., 1992) or higher order derivatives (Basu et al., 2013). Both interpolation and seismo-geodetic methods have been used for seismic dynamic and geodetic quasi-static strain estimates. While the single station procedure estimates the strain at the single position of the collocated sensor, the other two methods allow deriving a map of

65 strain on irregular grid points by making use of sensor array measurements. This makes the multiple station approach appropriate to estimate strain using dense seismic array methods and compare it with values derived from DAS along fibre cable.

Here, we extend the interpolation method proposed by Sandwell and Wessel (2016) and use the seismo-geodetic method in the formulation by Shen et al. (2015) in order to derive strain estimates from the dense seismic array data acquired at Etna.

70 The aim of the paper is twofold: (i) exploring the performance of interpolation and seismo-geodetic methods in deriving the strain field along a fibre optic cable and (ii) validating the DAS measurements acquired during the experiment at Etna volcano.

## 2 Data set

We designed the experiment in Piano delle Concazze at the Etna summit (Fig. 1) in order to test the potential of the DAS technology in a volcano-seismology application.

75 Deployment of equipment on active and dangerous volcanoes is challenging due to harsh environment and danger associated with the volcanic activity. Piano delle Concazze is a large flat area (elevation of about 2800 m), on the northern upper flank of the Etna volcano dominated by the North East Crater. It is bounded by the upper extremity of the North-East Rift, a preferential pathway for magma intrusions due to its structural weakness (Andronico and Lodato, 2005), and by the rim of the depression of the Valle del Leone. The area is affected by several North South-trending faults, that result from the accommodation of the 80 extension exerted by the North-East Rift (Azzaro et al., 2012; Napoli et al., 2021). Therefore, Piano delle Concazze is an area where new methodology can be tested, close enough to the active craters to study volcanic processes (ca. 1.8 km away from the Etna summit craters) and yet safe.

In order to record strain changes related to volcanic activity, we jointly deployed in Piano delle Concazze (Fig. 1):

1. a 1.5 km long fibre connected to a DAS interrogator (“Ella”, an iDAS® from Silixa) set up in Pizzi Deneri 85 Observatory. We interrogated the fibre from 1 July to 23 September 2019. A long trench was dug to deploy the fibre cable at a depth of about 40 cm. At a sampling rate of 1 kHz the DAS acquired the strain rate along the axial direction of the cable with a spatial resolution of 2 m and a gauge length of 10 m. This results in a dataset of 824 channels distributed along the fibre path. The spatial calibration and locations of the fibre channels were determined by jumping at several points near the fibre with jumping locations determined by handy GPS. The position of the channels between two successive jump locations were 90 computed by linear interpolation.

2. a dense seismic array comprising 26 Trilium Compact – 120 s broadband sensors (interstation distance of about 70 m), distributed over an area of about 0.2 km<sup>2</sup> (Fig. 1). The sensors were placed at a depth of about 40 cm deep holes in the compacted pyroclastic deposit. A Cube digitizer was used to acquire the data at a sampling rate of 200 Hz.

We designed the broadband sensor distribution and the path of the fibre optic cable, such that we could compare both records 95 with several methods.

### 3 Methodology

We estimate the strain field from the seismic array data using two different algorithms. The first is a new spatial interpolation method, in which we extend the work presented in Sandwell and Wessel (2016). The second is the seismo-geodetic method in the formulation proposed by Shen et al. (1996; 2015). For both methods the description and the analysis are limited to the 2D domain, since the investigated area is almost flat. However, extension to 3D is straightforward.

#### 3.1 Spatial interpolation method

In the spatial interpolation method (SIM) proposed by Sandwell and Wessel (2016), the general solution of the horizontal displacement components  $u, v$  at any location  $\vec{r}$  within a N-element seismic array is given by:

$$105 \quad \begin{aligned} u(\vec{r}) &= \sum_{j=1}^N q(\vec{r} - \vec{r}_j) f_x^j + w(\vec{r} - \vec{r}_j) f_y^j \\ v(\vec{r}) &= \sum_{j=1}^N w(\vec{r} - \vec{r}_j) f_x^j + p(\vec{r} - \vec{r}_j) f_y^j \end{aligned} \quad (1)$$

where  $q, p, w$  are the analytical Green's functions (Sandwell and Wessel, 2016), which solve the quasi-static balance equation of an elastic body subjected to in-plane body forces  $\mathbf{f}_x, \mathbf{f}_y$  applied at the station location  $\vec{r}_j$ . The Green's functions read as:

$$110 \quad \begin{aligned} q(\vec{r}) &= (3 - v) \ln r + (1 + v) \frac{y^2}{r^2} \\ p(\vec{r}) &= (3 - v) \ln r + (1 + v) \frac{x^2}{r^2} \\ w(\vec{r}) &= -(1 + v) \frac{xy}{r^2} \end{aligned} \quad (2)$$

where  $r$  is the distance between the location  $\vec{r}$  and the  $\vec{r}_j$  station position and  $v$  is the Poisson's ratio. Starting from these deformation solutions we derive the strain field  $\boldsymbol{\varepsilon}$ , which read as:

$$115 \quad \begin{aligned} \varepsilon_x(\vec{r}) &= \sum_{j=1}^N \frac{\partial q(\vec{r} - \vec{r}_j)}{\partial x} f_x^j + \frac{\partial w(\vec{r} - \vec{r}_j)}{\partial x} f_y^j \\ \varepsilon_{xy}(\vec{r}) &= \frac{1}{2} \sum_{j=1}^N \left[ \frac{\partial q(\vec{r} - \vec{r}_j)}{\partial y} + \frac{\partial w(\vec{r} - \vec{r}_j)}{\partial x} \right] f_x^j + \left[ \frac{\partial w(\vec{r} - \vec{r}_j)}{\partial y} + \frac{\partial p(\vec{r} - \vec{r}_j)}{\partial x} \right] f_y^j \\ \varepsilon_y(\vec{r}) &= \sum_{j=1}^N \frac{\partial w(\vec{r} - \vec{r}_j)}{\partial y} f_x^j + \frac{\partial p(\vec{r} - \vec{r}_j)}{\partial y} f_y^j \end{aligned} \quad (3)$$

where the gradients of the functions  $q, p, w$  are given by:

$$\begin{aligned}
\frac{\partial q(r)}{\partial x} &= (3-\nu) \frac{x}{r^2} - 2(1+\nu) \frac{xy^2}{r^4} & \frac{\partial q(r)}{\partial y} &= (3-\nu) \frac{y}{r^2} + 2(1+\nu) \frac{yr^2 - y^3}{r^4} \\
\frac{\partial w(r)}{\partial x} &= -(1+\nu) \frac{yr^2 - 2x^2y}{r^4} & \frac{\partial w(r)}{\partial y} &= -(1+\nu) \frac{xr^2 - 2xy^2}{r^4} \\
\frac{\partial p(r)}{\partial x} &= (3-\nu) \frac{x}{r^2} + 2(1+\nu) \frac{xr^2 - x^3}{r^4} & \frac{\partial p(r)}{\partial y} &= (3-\nu) \frac{y}{r^2} - 2(1+\nu) \frac{x^2y}{r^4}
\end{aligned} \tag{4}$$

We determine the body forces, applied at the N locations of the array stations, so that they match the displacement data using  
120 Eq (1). Therefore, we solve for a set of N vector body forces  $\mathbf{f}_x, \mathbf{f}_y$  with  $j=1\dots N$ , by setting up a  $2N \times 2N$  linear system of equations constrained by the horizontal displacement field recorded by the broadband seismic array. By solving the linear system, the body forces are determined and the components of the strain tensor can be computed at the location of the fibre channel using Eq (3). To avoid the singularity in the computation of the Green's functions (Eqs. 4), a  $\Delta r$  distance factor is added to the distance term (Sandwell and Wessel, 2016).

125 **3.2 Seismo-geodetic method**

The seismo-geodetic method (SGM) is based on the Taylor expansion of the displacement field and has been applied using different assumptions and strategies which lead to very similar formulations (Spudich et al., 1995; Shen et al., 1996; Teza et al., 2004; Langston and Liang, 2008; Basu et al., 2013; Langston et al., 2018). Here, we follow the formulation proposed in Teza et al. (2004). The displacement components  $u_i(x_k, y_k)$  with  $i=x, y$ , recorded at the  $k$ -th station are expanded with first  
130 derivative terms as:

$$u_i(x_k, y_k) \approx u_i(x_p, y_p) + \frac{\partial u_i}{\partial x}(x_k - x_p) + \frac{\partial u_i}{\partial y}(y_k - y_p) \tag{5}$$

where the first term  $u_i(x_p, y_p)$  is the  $i$ -th displacement component and the second and the third terms are the gradient displacements at a point  $P(x_p, y_p)$ , respectively. By computing this expression for the N stations of the array, a linear system of N equations is derived,  $\mathbf{Gm} = \mathbf{d}$ , whose solution provides the displacements and their gradient at the point P. If the  
135 displacement gradients are rewritten in terms of symmetric and rotational strain components, the system of equations read as (Shen et al., 2015):

$$\mathbf{G} = \begin{bmatrix} 1 & 0 & \Delta x_1 & 0 & \Delta y_1 & \Delta y_1 \\ 0 & 1 & 0 & \Delta y_1 & \Delta x_1 & -\Delta x_1 \\ \dots & \dots & \dots & \dots & \dots & \dots \\ \dots & \dots & \dots & \dots & \dots & \dots \\ 1 & 0 & \Delta x_N & 0 & \Delta y_N & \Delta y_N \\ 0 & 1 & 0 & \Delta y_N & \Delta x_N & -\Delta x_N \end{bmatrix}$$

$$\mathbf{m} = [u_x \ u_y \ \varepsilon_x \ \varepsilon_y \ \varepsilon_{xy} \ \omega]^T \quad (6)$$

$$\mathbf{d} = \begin{bmatrix} u_x(x_1, y_1, z_1) \\ u_y(x_1, y_1, z_1) \\ \dots \\ u_x(x_N, y_N, z_N) \\ u_y(x_N, y_N, z_N) \end{bmatrix}$$

140

The vector of the unknowns  $\mathbf{m}$  ( $T$  indicates the transposition operator) is composed of the horizontal displacements, the strain tensor components and the rotation. The vector  $\mathbf{d}$  is formed by the observed displacements at the stations of the array and  $\Delta x_i$  and  $\Delta y_i$  are the relative positions between the  $i$ -th station and the point P. In the first order Taylor expansion, the computed  
145 displacement gradients are constant (Basu et al., 2013; Shen et al., 2015) and, hence, the estimated strain tensor is spatially uniform over the entire extent of the array. Therefore, this method provides one representative value within the whole seismic array. To overcome this limit, a distance-weighted approach is introduced which locally weights the data on the basis of the relative distance  $R_i$  between the station and the point P (Shen et al., 2015). The diagonal terms of the weighting matrix are  
150 computed as exponential functions  $W_i = \exp\left(-\frac{R_i^2}{D^2}\right)$  where  $D$  is a spatial smoothing parameter. The system of equations is solved using a weighted least square approach  $\mathbf{m} = (\mathbf{G}^T \mathbf{W} \mathbf{G})^{-1} \mathbf{G}^T \mathbf{W} \mathbf{d}$ . The advantage of this method with respect to the Spudich formulation (1995) is that the displacement and the strain fields can be interpolated at any point P within the array without the need for defining a reference station.

### 3.3 Strain computations along fibre cable axial direction

Using one of the above methods, the strain tensor is computed at all channels of the fibre and it is projected along the local  
155 fibre direction to compute the local axial strain. Both procedures are iterated at each time step to obtain the time series of dynamic strain at all the channels of the fibre using the time series of the seismic array.

The accuracy of the array-derived strain estimates is limited by the inter-station distance  $L$ . The error of the strain estimate is given by  $e = 1 - \frac{\sin(\pi L/\lambda)}{\pi L/\lambda}$  where  $\lambda$  is the signal wavelength (Bodin et al., 1997; Spudich and Fletcher, 2008). Therefore, an  
160 accuracy of 90% is achievable if the dominant wavelength is larger than about four times the inter-station distance (Spudich and Fletcher, 2008 and reference therein). Considering that in Piano delle Concazze, the average apparent velocity  $V_a$  is not greater than 2 km/s (Saccorotti et al., 2004), we can deduce that the strain estimates can be derived from the seismic array data with a good accuracy up to a frequency  $f_{max} = V_a / 4\Delta$ , i.e. of about 7 Hz, for the average station distance of 70 m. It is worth noting that the accuracy of the solution is dependent on the factor  $\frac{\sin(\pi L/\lambda)}{\pi L/\lambda}$ , that is the same multiplicative factor giving the DAS response to axial strain over a gauge length of  $L$  (Bakku, 2015). This multiplicative factor comes, however, from two

165 independent analyses based on the estimate of strain under spatially uniform approximation (Spudich and Fletcher, 2008) for the interpolation methods and on the computation of average strain over a gauge length L (Bakku, 2015).

The SIM and SGM depend on the choice of some parameters which need to be tuned in order to obtain optimal solutions. They are the Poisson ratio and the  $\Delta r$  distance factor for SIM, and the spatial smoothing parameter for SGM. For both methods, the parameters are tuned by performing a simple grid search with the aim to improve the fitting between observed and estimated  
170 strain. When comparison with direct measurements of strain cannot be carried out, the tuning is performed on the deformation/velocity data, by a “boot-strapping” method, i.e., omitting one sensor from the computation and then, after calculating the displacement/velocity at the same station, the recorded and interpolated displacements/velocities are compared (Paolucci and Smerzini, 2008). For the SIM, the more sensitive smoothing parameter is the distance factor introduced to avoid singularities in the analytical solutions. The smaller it is, the sharper the solution. For the SGM, the smoothing parameter D  
175 weights the relative contribution of the station with distance in the weighted least square inversion. The smaller it is, the lesser the influence of the station at larger distance. So both of them locally average displacement/velocity and filter the signal as a function of wavelength. Smaller distance smoothing parameters are adapted for shorter wavelengths, whereas larger ones may perform better for longer wavelengths.

## 180 4 Results

During the acquisition period, the Etna volcano activity was mainly characterized by discontinuous strombolian explosions and isolated ash emissions from most of the active summit craters (North East, New South East, Bocca Nuova and Voragine), distant about 2 km from Piano delle Concazzze (Fig. 1). These activities, occurring at fluctuating intensity, preceded and accompanied the short-lived effusive eruptions on 18 and 27 July 2019 from the New South East Crater (NSEC), and continued  
185 until the end of the experiment. A wide variety of signals have been recorded, among which volcanic tremor, LP events, volcanic explosion, teleseismic and local seismic events. In order to validate the DAS records with the above described approaches, here we focus our analysis on classes of events with a frequency content less than 6 Hz. Among the several signals, we selected two types of events (Fig. 2): (i) a volcanic explosion (VE) accompanying the strombolian activity at NSEC on 6 July 2019 and (ii) a long period event (LP) on 27 August 2019 preceding the intensification of the eruptive activity at the  
190 summit craters in early September 2019. In agreement with other similar events recorded at Etna (Cannata et al., 2009), the spectra show frequency contents in the range 0.1 to 1 and 1 to 5 Hz for the LP and the VE events, respectively. Both broadband and DAS signals are filtered with a 3rd order Butterworth filter. The integration of DAS data over time provides the strain along the fibre optic cable. Data are down-sampled from 1 kHz to 200 Hz for direct comparison with strain derived from broadband array signals.

195 Some of the broadband seismometers (e.g. Bb02, Bb03, Bb04) are collocated with the fibre optic cable (distance of less than 1 m). This configuration enables also to apply the single station method, which, under the plane wave assumption, relates the

DAS strain at the nearest channel with the broadband particle velocity as  $\varepsilon_x = -pu_x$ , where  $\varepsilon_x$ ,  $u_x$  and  $p$  are the strain, the particle velocity and the horizontal slowness (i.e. the inverse of the apparent wave propagation velocity) along the cable axial direction  $\vec{x}$ , respectively. In Figure 2 we report the comparison between the DAS strain at the nearest channel, here channel 200 501, and the particle velocity at the station Bb04. A horizontal slowness of about 1 s/km is estimated to optimally scale the particle velocity and match with the strain. For both events a generally good agreement is achieved (Fig. 2 b and d). This single station method is appropriate to estimate the strain only at the position where the seismometer and the cable are collocated. Because of the high spatial variability of the strain along the fibre optic cable (Fig. 2), we attempt to estimate the strain at all channels using the multiple station methods described in the previous section.

205 Velocity data are first integrated over time to derive the displacement field, which is then used in the SIM and SGM methods. Residuals, in terms of RMSE (Root Mean Square Error) misfits, are computed between DAS strain measurements and the strain derived from the seismic array. The RMSE values computed along the fibre gives a local estimate of their respective discrepancy (Figs 3 and 4).

The SGM depends strongly on the spatial smoothing parameter D (see above). Therefore, we performed several computations 210 by varying the D parameter and selected the value at which the cumulative RMSE is minimized (Fig. 5). A minimum RMSE is found with a D value of 75 m and 100 m for the VE and LP events, respectively. Similar exploration in the parameter space was performed for the SIM, which depends on the  $\Delta r$  distance factor. Here the best fit for  $\Delta r$  was found for a value of 20 m and 10 m for the VE and LP event, respectively. An additional search was also carried out on the Poisson's ratio to improve the fit. We tested a range of Poisson ratio from -1 (fully decoupled) to 0.25 and 0.5 (elastic) to 1.0 (incompressible). By 215 comparing the misfits, the solutions with a value of 0.25 was chosen.

An overall good match is achieved for both methods (SGM and SIM) along the fibre. Higher RMSE misfits concentrate at the corner points, where, the cable direction turns abruptly and the axial strain is locally disturbed. Larger misfits are also visible along the two nearly EW branches (channel 134-302; 449-787), where the strain wavefield (Fig. 2 and Figs. S1-S2) is more complex and amplified with respect to the nearly NS branch (channel 302-449). Furthermore, discrepancies are also observed 220 in regions where the fibre crosses fault zones (Figs. 3 and 4). The amplitude of the array-derived strain estimates in the fault zone is mostly underestimated.

## 5 Discussion

We investigated several methods for indirect strain estimates from dense seismic array data aiming at the assessment of DAS 225 records. After a straightforward recasting and derivation of equations, we compared the SIM and the SGM methods for the estimates of strain fields from dense array data, which, in similar forms, have been applied in several fields of seismology and geodesy. To our knowledge, these approaches are adapted and tested on DAS data here for the first time.

SIM and SGM offer some advantages over single station method. Both provide a direct comparison between strain data and their estimates from velocity data, without any assumption on the local phase seismic velocity as required by single station

procedure. Particularly, when media are dispersive, the assumption of a constant phase velocity is possibly prone with errors.

230 Usually, and especially in volcanic area, the estimate of a phase seismic velocity is challenging, because of the presence of strong heterogeneity and fractured zones. Particularly, in Piano delle Concrazze, the phase seismic velocity varies markedly along the fiber cable because of the local complex structural geology that is characterized by a lava flow succession interbedded with volcaniclastic products (Branca et al., 2011) and by sub-vertical North-South trending faults affecting the superficial layers up to a maximum depth of about 40 m (Azzaro et al., 2012; Napoli et al., 2021).

235 Indeed, our results highlight strong discrepancies between direct DAS measures and indirect strain estimates in coincidence of fault zones (Figs. 3, 4). Thanks to the high spatial resolution of the DAS records, it is possible to observe how soil structure small-scale heterogeneities affect strain. Local strain perturbations are much shorter in wavelength (few tens of meters) with respect to the wavelength resolution of the array ( $\lambda > 200$  m). The seismic wavefield is distorted by the local geological structural features with clear amplifications of strain in correspondence to fault zones (Fig. 2). This agrees with the 240 amplification of DAS strain observed in the proximity of faults in the DAS experiment carried out in Iceland (Jousset et al., 2018; Schantz, 2020) and at Etna (Jousset et al., submitted). These findings clearly show that complex site effects introduced by lateral heterogeneities may increase significantly the strain with respect to simplified evaluations, that may underestimate such effects severely. These findings emphasize the potential in the use of DAS technique to both characterize and monitor local strain in the vicinity of fault zones by providing a direct measure of strain at a spatial sampling unachievable even with 245 large-N arrays. However, local strain perturbations are not found at all the positions where the fibre cable crosses the fault systems (Figs. 3, 4). The cause of this dissimilar response of the ground is hindered from the limited geological characterization of the area. Further investigations with complementary geophysical exploration methods could help in understanding the different behaviour at different locations.

The discrepancies are higher for the shorter wavelength signal recorded during the VE event with respect to the LP event (Figs. 250 6, 7), for which good estimates are obtained at almost all channels (Figs. 4, 8). Indeed, as already noted in Currenti et al., (2020), explosive events excite more phases due to scattering and reflection on faults and layered geology (Figs. 2 and S1). The discrepancies are larger in the nearly EW branches, possibly due to the relative direction between the main structural geology and the cable branches. For the longer wavelengths (e.g. LP event), SIM and SGM (Fig. 6) perform better than the single station approach (Fig. 2). These findings conform to the estimate of the accuracy, which is dependent on the wavelength 255 signals.

We also attempt to investigate how the gauge length may average out the effect of the small-scale heterogeneities by virtually increasing the gauge length with a spatial average of DAS data. We report the analysis on the VE event (Figs. S3-S8), where the effect of increasing the gauge length from 10 to 30 and 100 m is more significant due to the higher frequency content. Indeed, as expected, at higher gauge lengths the shorter wavelengths are filtered out (Fig. S3, S6). We used two averaging 260 approaches: (i) a simple average over channels (Figs. S4, S7); (ii) a moving average with a shift of 1 channel (Figs. S5, S8). Also with a gauge length of 30 m, the simple average degrades the signals and the main phases are already lost. On the other hand, the moving average preserves the main signal but smooths out local scattering and reflections which are no more visible.

When computing the misfit with the array derived strain estimates (Figs. S4-S8), the localized anomalies (Fig. 3) in coincidence of the faults due to the small-scale heterogeneities are flattened and broaden. These findings confirm that the distortion of the  
265 strain field is very localized and difficult to be observed by traditional seismic array methods, which require deployment of very dense network along “well-chosen active faults and a good amount of luck” (Cao and Mavroeidis, 2019).

Both methods allow for estimating strain on points distributed irregularly exploiting all the available dataset instead of relying on a single point measure (Figs. 7, 8). Moreover, the derivation of the analytical strain solutions in the SIM: (i) avoids to use finite-difference scheme to derive strain from regular grid point distribution of displacements, and hence, (ii) provides the  
270 strain at any point of the investigated area once the body force coefficients have been estimated by solving the linear system of equations. This results in a greater accuracy.

Finally, the proposed approaches offer the possibility to combine seismic array data with DAS measures to derive a 2D map of the local strain of the investigated area. By recasting the system of linear equations, it is straightforward to include the DAS strain measures and perform a joint inversion.

## 275 6 Conclusions

The joint deployment of a DAS device and of a dense seismic array at Etna summit offers a unique opportunity to observe and quantify accurately strain changes related to volcanic activity. The data set recorded during summer 2019 showed the great potential of distributed fibre optic sensing in volcanic environment. To our knowledge this is the first time that tiny strain  
280 changes related to volcanic explosions and LP events have been clearly recorded by DAS technology opening new perspectives for its use in volcano monitoring. The high spatial sampling of DAS measurements confirms the high variability of strain variations in complex geology and may offer a great opportunity to study soil response. These findings also contribute in explaining the difficulties often encountered in interpreting local strain changes from single strainmeter observations. The indirect strain estimates derived by the dense seismic array match quite well with the direct DAS measurements. Our findings validate both the proposed methods and the accuracy of DAS measurements in sensing strain changes produced by volcanic  
285 processes.

**Code and data availability.** MATLAB scripts and data are available upon request to the corresponding Author.

**Author contributions.** PJ, CK and MW conceived and supervised the project. PJ, GC and RN were involved with the  
290 experiment planning. GC conceptualized this study and performed the analyses. All Authors contributed to the acquisition of the field data, the writing of the manuscript and the discussion of the results.

**Competing interests.** The Authors declare no competing interests

295 **Acknowledgements.** Broadband seismometers and data logger equipment are from the Geophysical Instrument Pool Potsdam (GIPP). This work received funding from the GeoForschungZentrum Potsdam and the Helmholtz Association. The experiment was also financially supported through the Trans National Activity “FAME” within the EUROVOLC project (EU grant agreement ID: 731070). Thanks are due to V. Parra and the INGV staff composed of S. Consoli, D. Contrafatto, G. Larocca, D. Pellegrino, M. Pulvirenti for their great help in the field work.

300 **References**

- Ajo-Franklin, J. B., Dou, S., Lindsey, N. J., Monga, I., Tracy, C., Robertson, M., Tribaldos, V. R., Ulrich, C., Freifeld, B., Daley, T., et al.: Distributed acoustic sensing using dark fiber for near-surface characterization and broadband seismic event detection, *Scientific reports*, 360 9, 1–14, 2019.
- Andronico, D., and Lodato, L.: Effusive Activity at Mount Etna Volcano (Italy) During the 20th Century: A Contribution to 305 Volcanic Hazard Assessment, *Nat. Hazards*, 36, 407–443, <https://doi.org/10.1007/s11069-005-1938-2>, 2005.
- Azzaro, R., Branca, S., Gwinner, K., and Coltell, M.: The volcano-tectonic map of Etna volcano, 1:100.000 scale: an integrated approach based on a morphotectonic analysis from high-resolution DEM constrained by geologic, active faulting and seismotectonic data. *Ital. J. Geosci. (Boll. Soc. Geol. It.)*, 131, 1, 153-170, <https://doi.org/10.3301/IJG.2011.29>, 2012.
- Bakku, S.K., 2015, Fracture characterization from seismic measurements in a borehole, PhD thesis, Massachusetts Institute of 310 Technology, MA, USA.
- Basu, D., Whittaker, A.S., and Costantinou, M.C.: Extracting rotational components of earthquake ground motion using data recorded at multiple station, *Earthquake Engng Struct Dyn*, 42, 451-468, <https://doi.org/10.1002/eqe.2233>, 2013.
- Basu, D., Whittaker, A. S., and Costantinou, M. C.: On the design of a dense array to extract rotational components of 315 earthquake ground motion, *Bull Earthquake Eng*, 15, 827–860, <https://doi.org/10.1007/s10518-016-9992-6>, 2017.
- Bodin, P., Gomberg, J., Singh, S. K., and Santoyo M.: Dynamic deformations of shallow sediments in the Valley of Mexico, part I: Three-dimensional strains and rotations recorded on a seismic array, *Bull. Seismol. Soc. Am.* 87, 528–539, 1997.
- Branca, S., Coltell, M., Groppelli, G. and Lentini, F.: Geological map of Etna volcano, 1:50,000 scale *Italian J. Geosciences*, 130 (3), 265–291, <https://doi.org/10.3301/IJG.2011.15>, 2011.
- Bonaccorso, A., Calvari, S., Del Negro, C., and Falsaperla, S.: Mt. Etna: Volcano Laboratory, *Geophys. Monogr. Ser.* 143, 320 369 pp., AGU, Washington, D. C., <https://doi.org/10.1029/GM143>, 2004.
- Cannata, A., Hellweg, M., Di Grazia, G., Ford, S., Alparone, S.: Long period and very long period events at Mt. Etna volcano: Characteristics, variability and causality, and implications for their sources, *Journal of Volcanology and Geothermal Research*, 187, 3-4, 3-4, <https://doi.org/10.1016/j.jvolgeores.2009.09.007>, 2009.
- Cao, Y., and Mavroelidis, G. P.: A Parametric Investigation of Near-Fault Ground Strains and Rotations Using Finite-Fault 325 Simulations, *Bulletin of the Seismological Society of America*, Vol. 109, No. 5, pp. 1758–1784, <https://doi.org/10.1785/0120190045>, 2019.

- 330 Currenti, G., Zuccarello, L., Bonaccorso, A., and Sicali, A.: Borehole volumetric strainmeter calibration from a nearby seismic broadband array at Etna volcano, *J. Geophys. Res.*, <https://doi.org/10.1002/2017JB014663>, 2017.
- 330 Currenti G., and Bonaccorso, A.: Cyclic magma recharge pulses detected by high-precision strainmeter data: the case of 2017 inter-eruptive activity at Etna volcano, *Scientific Reports*, <https://doi.org/10.1038/s41598-019-44066-w>, 2019.
- 335 Currenti, G., Jousset, P., Chalari, A., Zuccarello, L., Napoli, R., Reinsch, T., and Krawczyk, C.: Fibre optic Distributed Acoustic Sensing of volcanic events at Mt Etna, *EGU General Assembly 2020*, Online, 4–8 May 2020, EGU2020-11641, <https://doi.org/10.5194/egusphere-egu2020-11641>, 2020
- 340 Donner, S., Chin-Jen, L., Hadzioannou, C., Gebauer, A., Vernon, F., Agnew, D. C., Igel, H., Schreiber, U., and Wassermann, J.: Comparing Direct Observation of Strain, Rotation, and Displacement with Array Estimates at Piñon Flat Observatory, California, *Seismological Research Letters*, 88, 4, <https://doi.org/10.1785/0220160216>, 2017.
- 345 Gomberg, J., and Agnew, D.: The accuracy of seismic estimates of dynamic strains: An evaluation using strainmeter and seismometer data from Piñon Flat Observatory, California. *Bulletin of the Seismological Society of America*, 86(1A), 212–220, 1996.
- 350 Jousset, P., Reinsch, T., Ryberg, T., Blanck, H., Clarke, A., Aghayev, R., Hersir, G. P., Henninges, J., Weber, M., and Krawczyk, C. M.: Dynamic strain determination using fibre-optic cables allows imaging of seismological and structural features, *Nature Communications*, 9, 1–11, <https://doi.org/10.1038/s41467-018-04860-y>, 2018.
- 355 Jousset, P., Neuberg, J., Jolly, A.: Modelling low-frequency volcanic earthquakes in a viscoelastic medium with topography, *Geophys. J. Int.*, <https://doi.org/10.1111/j.1365-246X.2004.02411.x>, 2004.
- 360 Kumagai, H., Saito, T., O'Brien, G., and Yamashina, T.: Characterization of scattered seismic wavefields simulated in heterogeneous media with topography, *J. Geophys. Res.*, 116, B03308, <https://doi.org/10.1029/2010JB007718>, 2011.
- 365 Langston, C. A., and Liang, C.: Gradiometry for polarized seismic waves, *J. Geophys. Res.*, 113, B08305, <https://doi.org/10.1029/2007JB005486>, 2008.
- 370 Langston, C. A.: Calibrating dense spatial arrays for amplitude statics and orientation errors. *Journal of Geophysical Research: Solid Earth*, 123, 3849–3870. <https://doi.org/10.1002/2017JB015098>, 2018.
- 375 Lindsey, N. J., Rademacher, H., and Ajo-Franklin, J. B.: On the broadband instrument response of fiber-optic DAS arrays, *J. Geophys. Res. Solid Earth*, 125, <https://doi.org/10.1029/2019JB018145>, 2020.
- 380 Napoli, R., Currenti, G., and Sicali, A.: Magnetic signatures of subsurface faults on the northern upper flank of Mt Etna (Italy), *Annals of Geophysics*, 64, 1, PE108, <https://doi.org/10.4401/ag-8582>, 2021.
- 385 Palaseanu-Lovejoy, M., Bisson, M., Spinetti, C., Buongiorno, M. F., Alexandrov, O., Cerere, T.: Digital surface model of mt Etna, Italy, derived from 2015 Pleiades Satellite Imagery: U.S. Geological Survey data release, <https://doi.org/10.5066/P9IGLDYE>, 2020.
- 390 Paolucci, R., and Smerzini, C.: Earthquake-induced Transient Ground Strains from Dense Seismic Networks, *Networks. Earthquake Spectra*, 24(2), 453–470, <https://doi.org/10.1193/1.2923923>, 2008.

- 360 Reinsch, T., Thurley, T., Jousset, P.: On the mechanical coupling of a fiber optic cable used for distributed acoustic/vibration sensing applications - a theoretical consideration. - *Measurement Science and Technology*, 28, 12, 127003, <https://doi.org/10.1088/1361-6501/aa8ba4>, 2017.
- Saccorotti, G., Zuccarello, L., Del Pezzo, E., Ibanez, J., Gresta, S.: Quantitative analysis of the tremor wavefield at Etna Volcano, Italy, *J. Volcanol. Geotherm. Res.*, 136 223– 245, <https://doi.org/10.1016/j.jvolgeores.2004.04.003>, 2004.
- 365 Sandwell, D. T.: Biharmonic spline interpolation of GEOS-3 and SEASAT altimeter data, *Geophys. Res. Lett.*, 14, 139–142, <https://doi.org/10.1029/GL014i002p00139>, 1987.
- Sandwell, D. T., and Wessel, P.: Interpolation of 2-D vector data using constraints from elasticity, *Geophys. Res. Lett.*, 43, 10,703–10,709, <https://doi.org/10.1002/2016GL070340>, 2016.
- Schantz, A.: Earthquake Characterization Using Distributed Acoustic Sensing (DAS) in a Case Study in Iceland, MSc-thesis, 370 TU Berlin, 101pp., 2020.
- Shen, Z.-K., Jackson, D. D., and Ge, B. X.: Crustal deformation across and beyond the Los Angeles basin from geodetic measurements, *J. Geophys. Res.*, 101, B12, 27 957–27 980, <https://doi.org/10.1029/96JB02544>, 1996.
- Shen, Z.K., Wang, M., Zeng, Y., and Wang, F.: Optimal Interpolation of Spatially Discretized Geodetic Data, *Bulletin of the Seismological Society of America*, 105, 4, 2117–2127, <https://doi.org/10.1785/0120140247>, 2015.
- 375 Spudich, P., Steck, L. K., Hellweg, M., Fletcher, J., and Baker, L. M.: Transient stresses at Parkfield, California, produced by the M 7.4 Landers earthquake of June 28, 1992: observations from the UPSAR dense seismograph array, *J. Geophys. Res.* 100, 675–690, <https://doi.org/10.1029/94JB02477>, 1995.
- Spudich, P., and Fletcher, J.B.: Observation and Prediction of Dynamic Ground Strains, Tilts, and Torsions Caused by the Mw 6.0 2004 Parkfield, California, Earthquake and Aftershocks, Derived from UPSAR Array Observations, *Bulletin of the Seismological Society of America*, 98, 4, 1898–1914, <https://doi.org/10.1785/0120070157>, 2008.
- 380 Suryanto, W., Igel, H., Wassermann, J., Cochard, A., Schuberth, B., Vollmer, D., Scherbaum, F., Schreiber, U., and Velikoseltsev, A.: First comparison of array-derived rotational ground motions with direct ring laser measurements, *Bull. Seismol. Soc. Am.* 96, 2059–2071, <https://doi.org/10.1785/0120060004>, 2006.
- Teza, G., Pesci, A., and Galgaro, A.: Software packages for strain field computation in 2D and 3D environments, *Computers and Geosciences* 34, 1142–1153, <https://doi.org/10.1016/j.cageo.2007.07.006>, 2004.
- 385 Yu, C., Zhan, Z., Lindsey, N. J., Ajo-Franklin, J. B., and Robertson, M.: The potential of DAS in teleseismic studies: Insights from the Goldstone experiment. *Geophysical Research Letters*, 46, 1320–1328, <https://doi.org/10.1029/2018GL081195>, 2019.
- Wang, H. F., Zeng, X., Miller, D. E., Fratta, D., Feigl, K. L., Thurber, C. H., and Mellors, R. J.: Ground motion response to an 390 ML 4.3 earthquake using co-located distributed acoustic sensing and seismometer arrays, *Geophysical Journal International*, 213, 2020–2036, <https://doi.org/10.1093/gji/ggy102>, 2018.
- Wessel, P., and Bercovici, D.: Interpolation with splines in tension: A Green's function approach, *Math. Geol.*, 30, 1, 77–93, <https://doi.org/10.1023/A:1021713421882>, 1998.



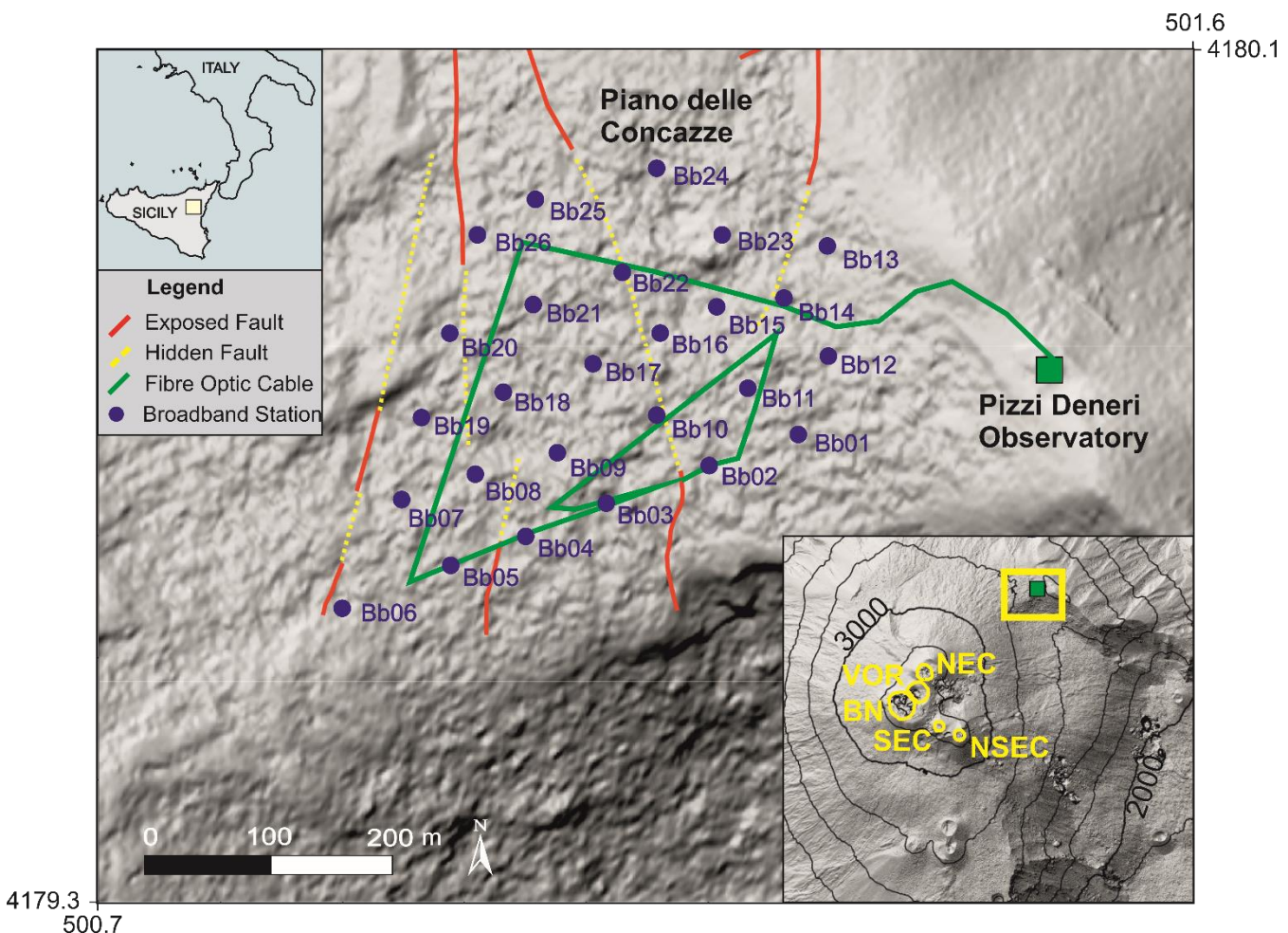
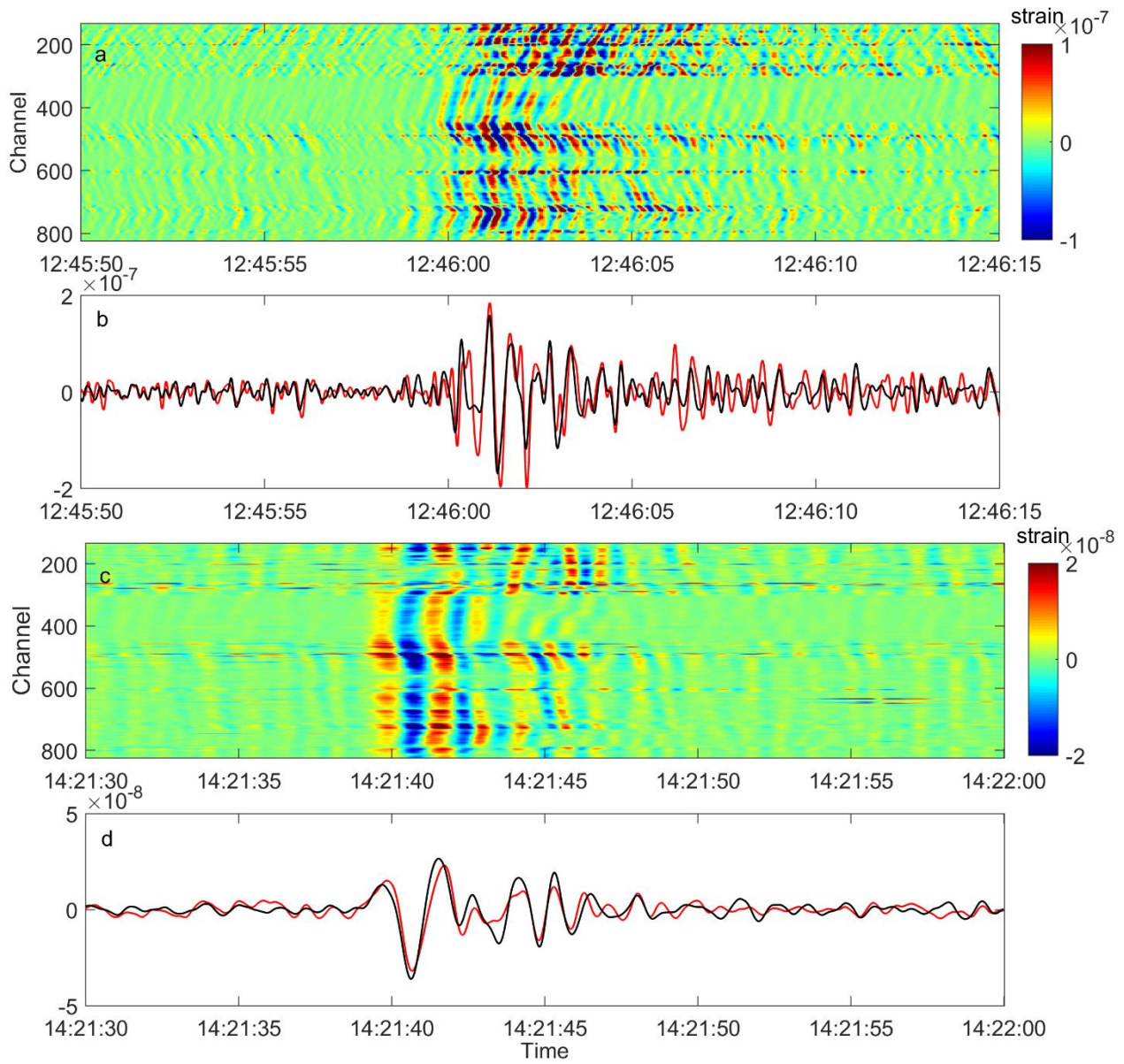


**Figure 1:** Digital terrain model of Piano delle Concazze in the North-East flank of Etna volcano (Palaseanu-Lovejoy et al., 2020) with the dense broadband seismic array (26 stations; Bb01-Bb26) and the Distributed Acoustic Sensing (DAS) cable layout. The DAS cable geometry is designed in order to record dynamic strain changes along several directions. No data were recorded by the station Bb05 because of technical problem. The DAS interrogator was hosted inside the Pizzi Deneri Observatory, that is about 2 km away from the five summit craters (North-East: NEC, Voragine: VOR, Bocca Nuova: BN, South-East: SEC, New South-East: NSEC). The investigated area, almost flat, is crossed by a sub-vertical fault system (redrawn after Azzaro et al., 2012). Geographic coordinates (in km) are in UTM33S system.



410 **Figure 2:** Time series of DAS strain during a small volcanic explosion (VE) at Etna on 6 July 2019 (a, b) and during a long-period (LP) event on 27 August 2019 (c, d). The DAS strain is computed by integrating over time the DAS records. Data are filtered in the frequency range 1 to 5 Hz for the VE event (a, b) and between 0.1 to 1 Hz for the LP event (c, d). (b, c) The broadband velocity at station Bb04 (black line in b and d), located in proximity of the DAS channel 501, are projected along the cable direction to compare the data using the single station procedure. An average scaling factor of 1s/km for the slowness value is found in both cases.

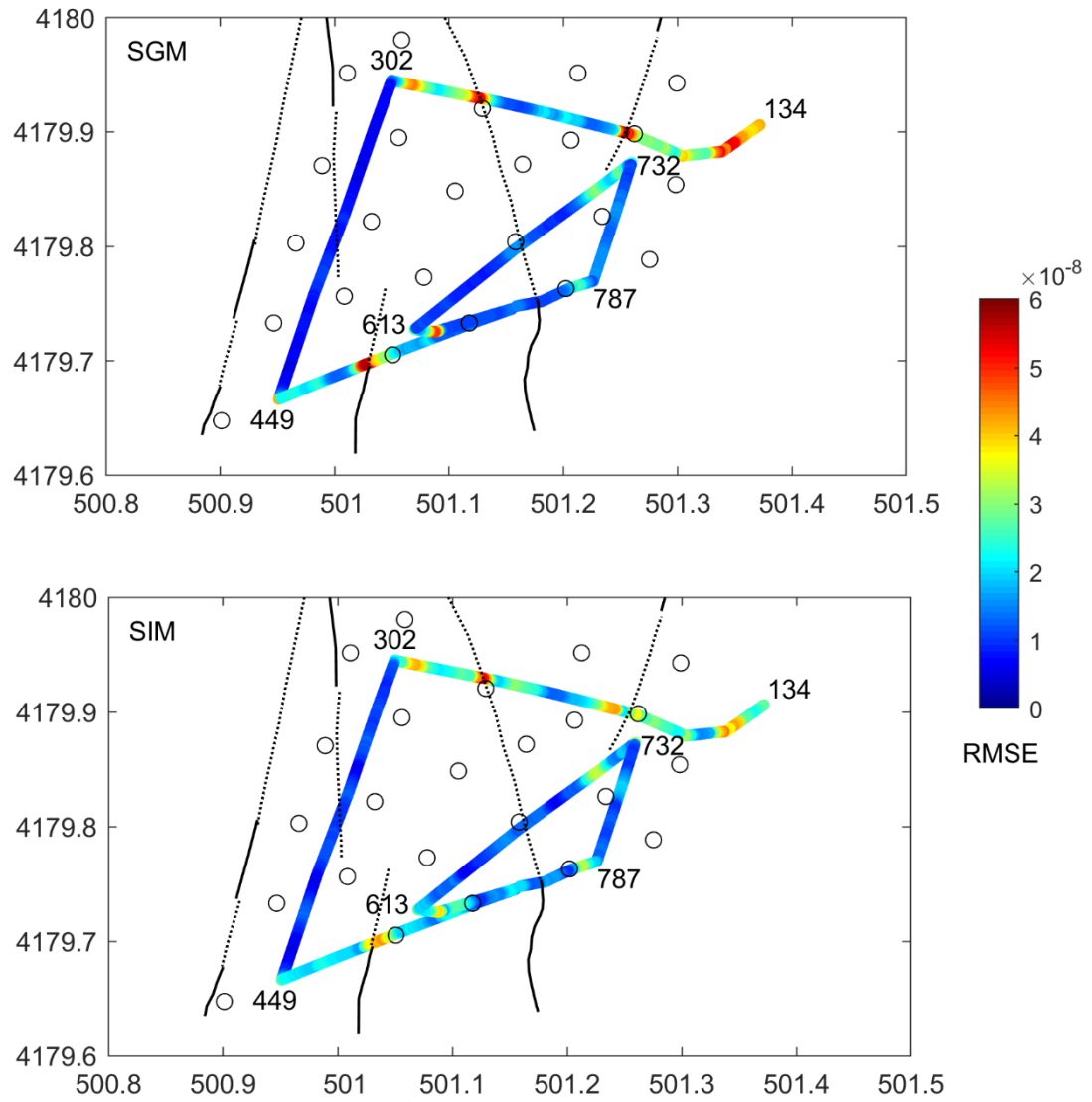


**Figure 3:** RMSE residuals between DAS strain measurements (Fig. 2a) and the strain derived from the seismic array along the fibre for the VE event. (Top) DAS vs. the seismo-geodetic method (SGM). (Bottom) DAS vs. the spatial interpolation method (SIM). Black lines and open circles indicate faults and seismometers shown in Fig.1, respectively. For more details see text.

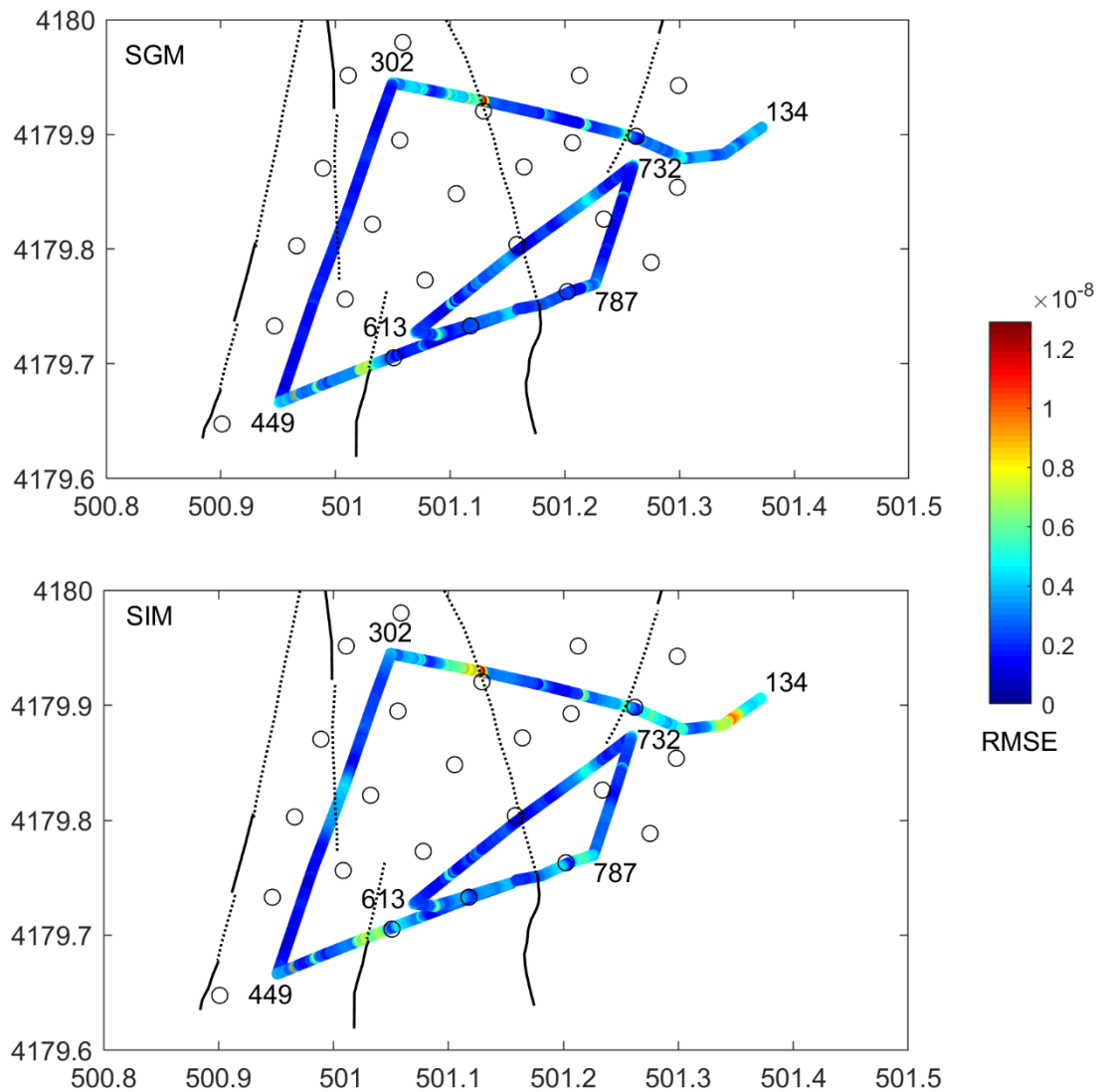
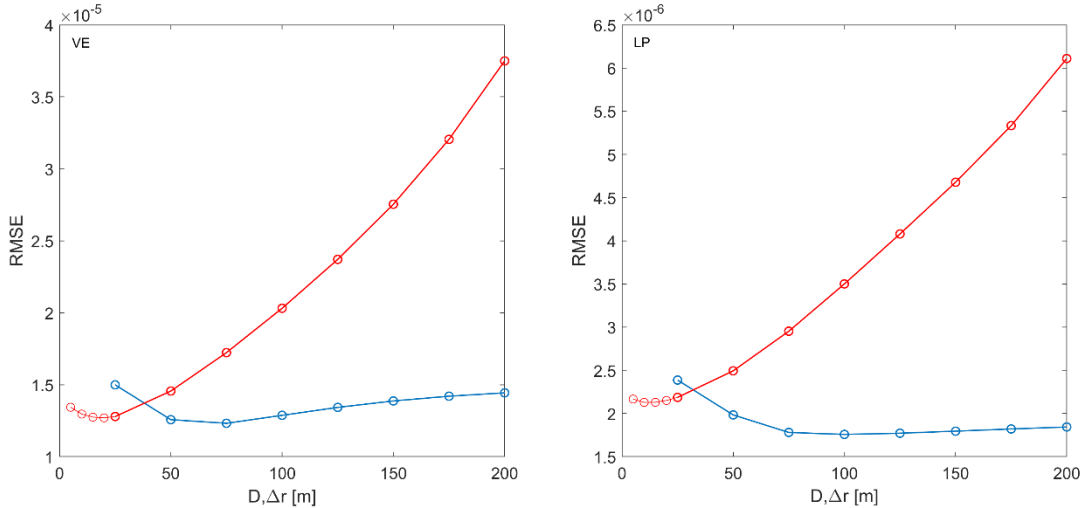


**Figure 4:** RMSE residuals between DAS strain measurements (Fig. 2c) and the strain derived from the seismic array along the fibre for the LP event. Black lines and open circles indicate faults and seismometers shown in Fig. 1, respectively.



425

**Figure 5:** Cumulative residuals over all fibre channels between DAS strain measurements and strain derived from SGM (blue line) and from SIM (red line) for different smoothing parameters ( $D$  for SGM and  $\Delta r$  for SIM, respectively). Computations are performed for the VE (left) and LP (right) events, respectively.

430

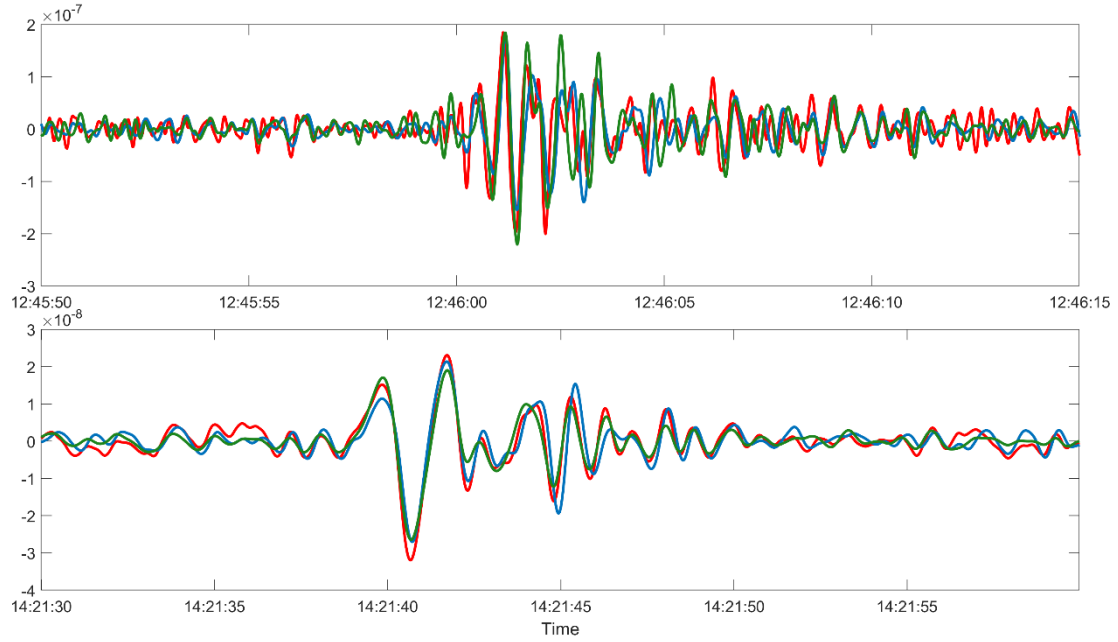


**Figure 6:** Array-derived strain estimates at station Bb04 (Fig. 1) using the SIM (green line) and the SGM (blue line) in comparison with DAS strain data (red line). Computations are performed for the VE (top) and LP (bottom) events.

435

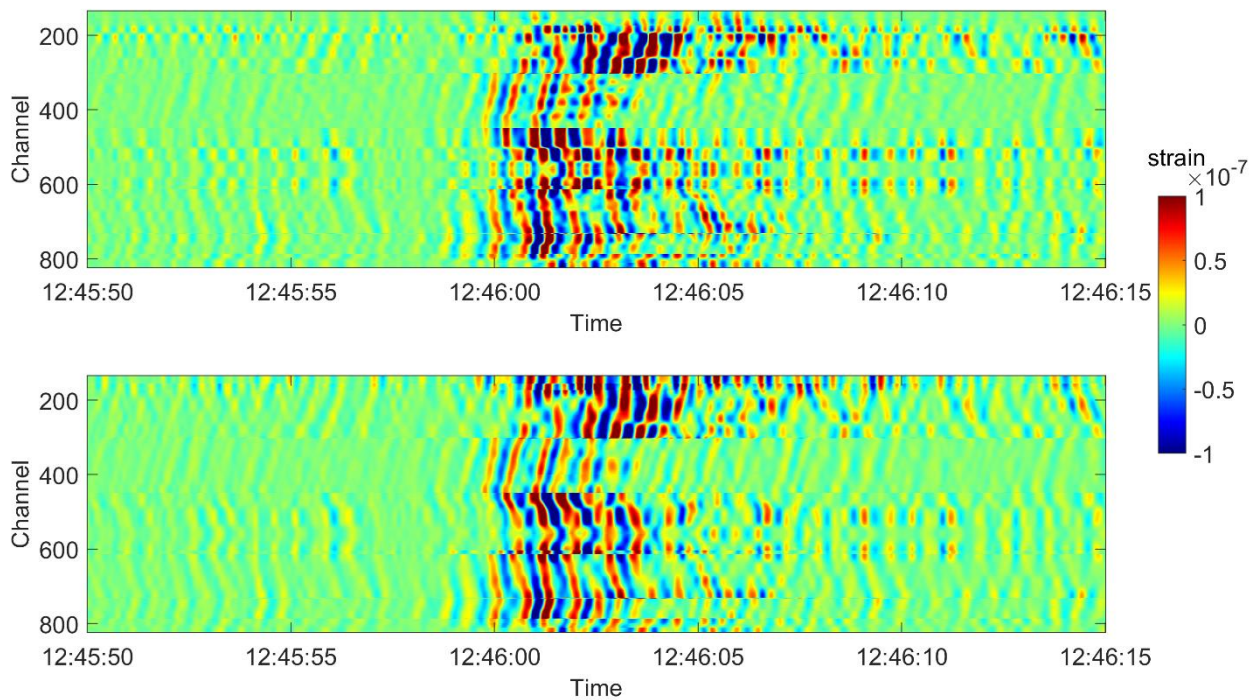


**Figure 7:** – Strain estimates over all fibre channels using SGM (top) and SIM (bottom) for the VE event. The solutions with the minimum RMSE are chosen, respectively (Fig. 5).

440

445

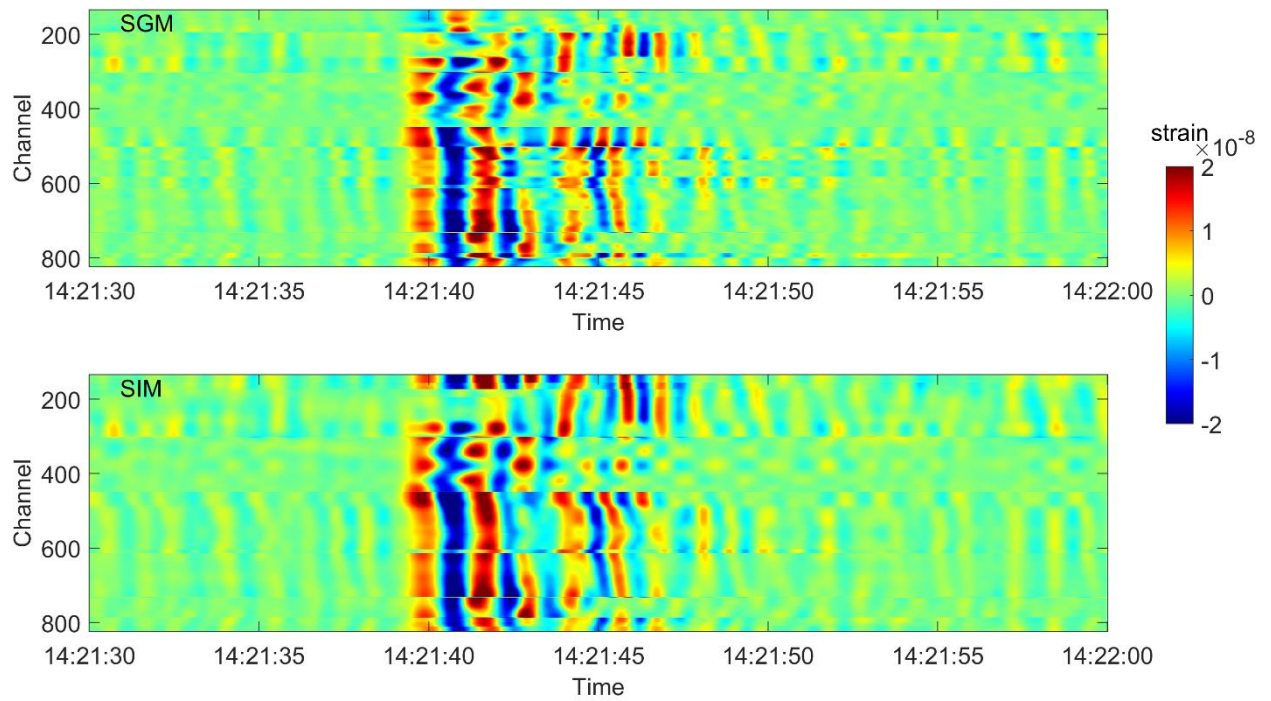


**Figure 8:** Strain estimates over all fibre channels using SGM (top) and SIM (bottom) for the LP event. The solutions with the minimum RMSE are chosen, respectively (Fig. 5).

450